AIAA JOURNAL
Vol. 40, No. 11, November 2002

Computation of Trailing-Edge Noise Due to Turbulent Flow over an Airfoil

Assad A. Oberai,* Farzam Roknaldin,† and Thomas J. R. Hughes‡
Stanford University, Stanford, California 94305-4040

Application of the variational formulation of Lighthill's acoustic analogy to trailing-edge noise is considered. Use is made of this formulation to study the effect of finiteness of the chord and the variation of far-field pressure directivity with frequency. Numerical analytical solution results are validated for certain limiting cases. Use is also made of this methodology to calculate the far-field acoustic pressure for a low-Mach-number turbulent flow. To determine the acoustic sources for this problem, we employ an unstructured mesh, large eddy simulation of the incompressible Navier–Stokes equations.

Nomenclature

a	=	radius of the quadrupole source in model problem
a_n	=	coefficients in the exterior expansion of pressure
C	=	sound speed in quiescent medium
C_p	=	time-averaged pressure coefficient
e	=	exponential function
f	=	acoustic source term, $\nabla \cdot (\nabla \cdot \boldsymbol{T})$
H	=	Heaviside function
H^1	=	Sobolev space of functions with first derivatives
$H_n^{(1)}$	=	Hankel function of the first kind
i	=	$\sqrt{-1}$
k	=	nondimensional wave number, ωM
k_γ	=	modified wave number, $\sqrt{(k^2 - \gamma^2)}$
L	=	chord length
M	=	Mach number
$\boldsymbol{n}$	=	unit outward normal, (n_x, n_y, n_z)
p	=	fluid pressure
p_C	=	incompressible solution of the model quadrupole problem
p_D	=	diffracted component of acoustic pressure
p_I	=	incident component of acoustic pressure
p_R	=	reflected component of acoustic pressure
p_S	=	scattered component of acoustic pressure
$\boldsymbol{R}_0$	=	center of quadrupole sources
Re	=	Reynolds number, $\rho_\infty u_\infty L/\mu$
r	=	radial coordinate, $\sqrt{(x^2 + y^2 + z^2)}$
$\bar{r}$	=	radial coordinate, $\sqrt{(x^2 + y^2)}$
S	=	Dirichlet-to-Neumann map
$\boldsymbol{T}$	=	Lighthill's turbulence tensor
T_{ij}	=	components of Lighthill's turbulence tensor
$\boldsymbol{u}$	=	fluid velocity vector, $(u, v, w) = (u_1, u_2, u_3)$
u_τ	=	skin-friction velocity
u_∞	=	freestream fluid velocity
$\mathcal{V}$	=	space of weighting functions and trial solutions
w	=	weighting functions
(x, y, z)	=	right-handed coordinate system
Γ	=	wet surface of the airfoil
$\bar{\Gamma}$	=	(x, y) extent of the wet surface of the airfoil
$\bar{\Gamma}_R$	=	truncating curve
γ	=	spanwise wave number
δ	=	Dirac distribution
θ	=	polar angle, $\tan^{-1}(y/x)$
λ	=	acoustic wavelength
μ	=	viscosity
ρ_∞	=	mean fluid density
Ω	=	domain exterior to the airfoil
$\bar{\Omega}$	=	(x, y) extent of the domain exterior to the airfoil
$\bar{\Omega}_R$	=	truncated two-dimensional domain exterior to the airfoil
ω	=	nondimensional angular frequency
$(\cdot\,,\cdot)$	=	L_2–inner product on $\bar{\Omega}_R$
$(\cdot\,,\cdot)_{\Gamma_R}$	=	L_2–inner product on $\bar{\Gamma}_R$
$\langle\cdot\rangle$	=	spanwise and time average
$\otimes$	=	outer product symbol

Superscripts

$\tilde{}$	=	Fourier transform in time
$\hat{}$	=	Fourier transform in time and spanwise coordinate

Introduction

THE problem of noise generated by turbulent flows over structures is important in the design of submarines, surface ships, airplanes, and automobiles. A canonical problem that occurs in several of these application areas is one of noise generated by low-Mach-number, turbulent flow over a lifting surface (a hydrofoil or airfoil). For this problem, the trailing edge of the airfoil plays an important role in the propagation of noise to the far field, and thus, the problem is commonly referred to as the trailing-edge noise problem. In this paper, we solve this problem using a computational acoustics formulation developed in our previous work.[1]

Low-Mach-number aeroacoustic problems are solved efficiently employing Lighthill's acoustic analogy.[2,3] In this approach, the original problem is decomposed into two parts, one that involves the solution of the Navier–Stokes equations to determine the unsteady fluid variables and another that involves the solution of an acoustic problem driven by quadrupole sources whose distribution is determined by the components of Lighthill's turbulence tensor. This tensor is constructed from the unsteady flowfield computed in the fluid calculation. If the effect of compressibility is retained in the fluid calculation, then the acoustic problem may be solved using the Ffowcs Williams and Hawkings equation.[4] This equation requires only the knowledge of the free-space acoustic Green's function and may be used to solve problems involving structures with complex geometry with relative ease. For an application of Ffowcs Williams and Hawkings equation to the trailing-edge noise problem, the reader is referred to Refs. 5 and 6.

From a computational standpoint, it is often preferable to ignore the effects of compressibility for low-Mach-number turbulent flows and to solve the incompressible Navier–Stokes equations to

Received 12 October 2001; revision received 21 May 2002; accepted for publication 29 May 2002.

*Postdoctoral Research Associate, Division of Mechanics and Computation; currently Assistant Professor, Department of Aerospace and Mechanical Engineering, Boston University, Boston, MA 02215; oberai@bu.edu. Member AIAA.

†Graduate Research Assistant, Division of Mechanics and Computation.

‡The Mary and Gordon Crary Family Professor of Engineering and Chairman, Division of Mechanics and Computation.

construct Lighthill's turbulence tensor. The advantages of doing so are twofold. First, an incompressible turbulent calculation (using large-eddy simulation, for instance) is computationally less intensive than a corresponding compressible calculation. Second, this leads to a formulation wherein the effect of compressibility appears only in the acoustic equations. Thus, to determine the acoustic response for a range of sufficiently small Mach numbers, the same Lighthill's tensor may be utilized in the acoustic analogy, thereby implying that only a single fluid calculation need be performed. This significantly reduces the computational effort associated with the overall analysis.

For cases where Lighthill's tensor is constructed from incompressible fluid calculations, the application of the Ffowcs Williams and Hawkings equation yields incorrect acoustic results except in the long wavelength limit. (For a discussion, see Refs. 6 and 7.) To solve the acoustic problem consistently, it becomes necessary to treat the structure as "sound-hard." Typically this is accomplished by constructing and using sound-hard Green's functions for simplified structures that approximate the geometry of the original structure. Clearly the accuracy of the solution obtained using this approach is limited by the approximations incurred when simplifying the original structure. The reader is referred to Refs. 7–12 for applications of this approach to the trailing-edge noise problem. An approach where no such assumptions are made was proposed by Oberai et al.[1] In this approach, a variational formulation of Lighthill's acoustic analogy was developed and solved numerically using the finite element method. In addition to modeling complex structures, this methodology allowed for the structure to be flexible. In the present paper, we consider the application of this approach to the trailing-edge noise problem when the airfoil is treated as sound-hard.

We consider two problems. In the first problem, we use simplified quadrupole sources to investigate the effect of finite chord on far-field noise and the variation of far-field pressure directivity as function of frequency. In the second problem, we use a distribution of quadrupole sources obtained by solving the incompressible Navier–Stokes equations for a turbulent flow to determine far-field acoustic pressure. In the fluid calculation, we use large-eddy simulation (LES) to model turbulence. The philosophy of LES is to solve the filtered Navier–Stokes equations for the relatively large, energetic scales of turbulence and to model the effect of unresolved scales (so-called subgrid scales) on the resolved scales. The fluid calculation yields velocities varying in space and time that are used to construct Lighthill's turbulence tensor. This approach of using an LES calculation to construct sources for the acoustic problem is relatively new. (For precedents, see Refs. 13–15.) The advantage of this approach over using turbulent wall-pressure spectra models is its applicability to flows with complex features such as separation, reattachment, and turbulent boundary layers under adverse pressure gradients. The example problem under consideration contains all of these features.

Our solution of the trailing-edge noise problem is novel in the following aspects:

1) In the acoustic problem, noise sources are determined using LES, and at the same time full account is taken of the finiteness of the chord. Previous studies have incorporated only one of these two aspects.

2) Previous studies that do take into account the finiteness of the chord (for example, Ref. 12) do not model the effect of the detailed geometry. In our approach, such effects are included because the geometry of the airfoil is not simplified when solving the acoustic problem.

The remainder of this paper is organized as follows. In the following section, we describe the overall problem formulation and a simplification in the acoustic problem that results when calculating the far-field pressure. Thereafter, we solve a trailing-edge noise problem with simplified acoustic sources, followed by the calculation of noise induced by turbulent flow over an airfoil. We end with concluding remarks.

Problem Formulation

We wish to calculate noise generated by low-Mach-number unsteady/turbulent flows over an airfoil. Using Lighthill's acoustic analogy, this problem is split into two parts. First, we solve the incompressible Navier–Stokes equations over a time interval of interest given by $(0, T)$, to determine the unsteady velocity field. These equations are given by

$$\boldsymbol{u}_{,t} + \nabla \cdot (\boldsymbol{u} \otimes \boldsymbol{u}) = -\nabla p + (1/Re)\nabla^2 \boldsymbol{u} + \boldsymbol{f} \qquad \text{in} \quad \Omega \tag{1}$$

$$\nabla \cdot \boldsymbol{u} = 0 \qquad \text{in} \quad \Omega \tag{2}$$

along with appropriate boundary and initial conditions. We let x denote the streamwise direction, let z denote the spanwise direction, and select y so that (x, y, z) forms a right-handed Cartesian coordinate system. The center of the coordinate system is chosen so that the trailing edge of the airfoil is on the line $(0, 0, z)$, $z \in (-\infty, \infty)$. Furthermore, in Eqs. (1) and (2), $\boldsymbol{u} = (u_1, u_2, u_3) = (u, v, w)$ is the velocity vector, nondimensionalized by the freestream velocity u_∞ and p is the pressure, nondimensionalized by $\rho_\infty u_\infty^2$.

After integrating Eqs. (1) and (2) in time, we solve for $\tilde{p}$, the Fourier transform of the acoustic pressure p. The equations for $\tilde{p}$ for a given nondimensional angular frequency ω are given by (details in Refs. 1 and 2)

$$-\nabla^2 \tilde{p} - k^2 \tilde{p} = \tilde{f} = \nabla \cdot (\nabla \cdot \tilde{\boldsymbol{T}}) \qquad \text{in} \quad \Omega \tag{3}$$

$$\nabla \tilde{p} \cdot \boldsymbol{n} = 0 \qquad \text{on} \quad \Gamma \tag{4}$$

$$\lim_{r \to \infty} r\left(\frac{\partial \tilde{p}}{\partial r} - ik\tilde{p}\right) = 0 \tag{5}$$

where $\boldsymbol{T}$ is Lighthill's turbulence tensor, whose components are given by

$$T_{ij} = u_i u_j \tag{6}$$

and a tilde over a quantity indicates its Fourier transform with respect to time.

Remark: For the given problem, Ω and Γ may be separated as

$$\Omega = \bar{\Omega} \times (-\infty, \infty) \tag{7}$$

$$\Gamma = \bar{\Gamma} \times (-\infty, \infty) \tag{8}$$

where $\bar{\Omega}$ is a two-dimensional domain exterior to $\bar{\Gamma}$, a curve that represents the profile of the airfoil. In the following development, we will make use of this decomposition to simplify the acoustic problem.

Far-Field Approximation

In the acoustic problem (3–5), the sound-hard boundary condition (4) is independent of the z coordinate, and the domain Ω and the surface Γ may be separated as in Eqs. (7) and (8), respectively. Hence, we may apply a Fourier transform in the z direction to simplify this problem. In the following development, we make use of this transform to arrive at a simplified version of the original acoustic problem for far-field pressure on the $z = 0$ plane.

For a given variable $\tilde{u}$, we let $\hat{u}$ denote its Fourier transform with respect to the z direction, that is,

$$\hat{u}(x, y, \gamma) = \int_{-\infty}^{\infty} \tilde{u}(x, y, z) e^{-i\gamma z}\, \mathrm{d}z \tag{9}$$

The Fourier transform of Eqs. (3–5) yields

$$-\left(\frac{\partial^2}{\partial x^2} + \frac{\partial^2}{\partial y^2}\right)\hat{p} - k_\gamma^2 \hat{p} = \hat{f} \qquad \text{in} \quad \bar{\Omega} \tag{10}$$

$$\frac{\partial \hat{p}}{\partial x} n_x + \frac{\partial \hat{p}}{\partial y} n_y = 0 \qquad \text{on} \quad \bar{\Gamma} \tag{11}$$

$$\lim_{\bar{r} \to \infty} \bar{r}^{\frac{1}{2}}\left(\frac{\partial \hat{p}}{\partial \bar{r}} - \mathrm{i}k_\gamma \hat{p}\right) = 0 \tag{12}$$

Outside a circle that encloses the airfoil, $\hat{p}$ can be expressed as

$$\hat{p}(\bar{r},\theta,\gamma)=\sum_{n=-\infty}^{\infty}a_n(\gamma)H_n^{(1)}(k_\gamma\bar{r})e^{in\theta} \tag{13}$$

where $H_n^{(1)}(x)$ represents the nth-order Hankel function of the first kind in the argument x and the coefficients $a_n(\gamma)$ are determined by solving Eqs. (10–12). Utilizing this representation and the definition of the inverse Fourier transform, we arrive at the following expression:

$$\tilde{p}(\bar{r},\theta,z)=\frac{1}{2\pi}\int_{-\infty}^{\infty}\left[\sum_{n=-\infty}^{\infty}a_n(\gamma)H_n^{(1)}(k_\gamma\bar{r})e^{in\theta}\right]e^{i\gamma z}\,\mathrm{d}\gamma \tag{14}$$

In the limit $x\to\infty$, Hankel functions may be expressed as

$$H_n^{(1)}(x)\approx c_n\left(e^{ix}/\sqrt{x}\right) \tag{15}$$

See, for example, Ref. 16, page 364. The exact value of c_n is not important to our development and will not appear in the final result. Utilizing this expression in Eq. (14) for $\bar{r}\to\infty$ and $z=0$, we arrive at

$$\tilde{p}(\bar{r},\theta,0)\approx\frac{1}{2\pi\sqrt{\bar{r}}}\sum_{n=-\infty}^{\infty}c_ne^{in\theta}\int_{-\infty}^{\infty}\frac{a_n(\gamma)}{\sqrt{k_\gamma}}e^{ik_\gamma\bar{r}}\,\mathrm{d}\gamma \tag{16}$$

In the limit $\bar{r}\to\infty$, the integrand of each integral in the preceding sum is the product of a slowly varying function, $a_n(\gamma)/\sqrt{k_\gamma}$, and a rapidly varying function, $e^{ik_\gamma\bar{r}}$. Thus, the method of stationary phase may be used to approximate this integral. The application of this method yields the following expression for $\tilde{p}$:

$$\tilde{p}(\bar{r},\theta,0)\approx\frac{e^{i\pi/4}}{\sqrt{2\pi}}\frac{e^{ik\bar{r}}}{\bar{r}}\sum_{n=-\infty}^{\infty}a_n(0)c_ne^{in\theta} \tag{17}$$

(See Junger and Feit,[17] pages 175, 176, for a similar development.) Also, for $\bar{r}\to\infty$, from Eqs. (13) and (15), we have

$$\hat{p}(\bar{r},\theta,0)\approx\frac{e^{ik\bar{r}}}{\sqrt{k\bar{r}}}\sum_{n=-\infty}^{\infty}a_n(0)c_ne^{in\theta} \tag{18}$$

which along with Eq. (17) yields

$$\tilde{p}(\bar{r},\theta,0)\approx\hat{p}(\bar{r},\theta,0)[(1+i)/2]\sqrt{k/\pi\bar{r}} \tag{19}$$

Thus, to calculate $\tilde{p}(\bar{r},\theta,0)$ in the far field, we first solve Eqs. (10–12) for $\gamma=0$ to obtain $\hat{p}(\bar{r},\theta,0)$ and then utilize Eq. (19).

Remark: The final result (19) provides a formula to calculate the far-field pressure for $z=0$ that replaces the solution of the original three-dimensional problem, namely, Eqs. (3–5), with a solution of a two-dimensional problem, namely, Eqs. (10–12) for $k_\gamma=k_0=k$.

Solving for $\hat{p}$

In Eqs. (10–12), $\hat{p}$ is the solution to an exterior acoustic problem wherein the structure is treated as sound-hard. To solve this problem for arbitrarily shaped structures, we use the methodology described in Ref. 1. We begin by posing an equivalent problem on a truncated domain $\bar{\Omega}_R$, namely,

$$-\left(\frac{\partial^2}{\partial x^2}+\frac{\partial^2}{\partial y^2}\right)\hat{p}-k_\gamma^2\hat{p}=\hat{f}\qquad\text{in}\quad\bar{\Omega}_R \tag{20}$$

$$\frac{\partial\hat{p}}{\partial x}n_x+\frac{\partial\hat{p}}{\partial y}n_y=0\qquad\text{on}\quad\bar{\Gamma} \tag{21}$$

$$\frac{\partial\hat{p}}{\partial x}n_x+\frac{\partial\hat{p}}{\partial y}n_y=S(\hat{p})\qquad\text{on}\quad\bar{\Gamma_R} \tag{22}$$

where $\bar{\Omega}_R$ is the domain enclosed within the truncating surface Γ_R and S is the Dirichlet-to-Neumann (DtN) map (see Ref. 18) that renders Eqs. (10–12) and Eqs. (20–22) equivalent. To solve this problem numerically, we construct an equivalent weak formulation: Find $\hat{p}\in\mathcal{V}=H^1(\bar{\Omega}_R)$, such that

$$(\nabla w,\nabla\hat{p})-k_\gamma^2(w,\hat{p})-(w,S(\hat{p}))_{\Gamma_R}=(\nabla w,\nabla\cdot\hat{\boldsymbol{T}}),\qquad\forall w\in\mathcal{V} \tag{23}$$

It is easy to see that the Euler–Lagrange equations implied by this equation are Eqs. (20–22).

We use the finite element method to approximate Eq. (23). To solve the resulting system of linear equations efficiently, and to avoid the penalties associated with the nonlocality of the DtN map, we use the quasi-minimal residual algorithm of Freund and Nachtigal[19] with a symmetric successive overrelaxation preconditioner, in conjunction with the efficient matrix–vector algorithms.[20]

Trailing-Edge Noise for a Model Source

In this section, we calculate the far-field acoustic pressure generated by a model quadrupole source placed near the trailing edge of an airfoil. The same airfoil is used in the following section to determine the noise generated by a turbulent flow. As described in the preceding section, this pressure is obtained first by solving Eq. (23) for $\hat{p}$, and then using Eq. (19) to obtain $\tilde{p}$. The airfoil chosen is the Eppler 387 at 2-deg angle of attack. The units of length are chosen such that the chord length is unity. The airfoil is assumed infinite in the spanwise direction.

The goals of this study are to validate our approach against analytical solutions, to illustrate the effect of airfoil geometry on far-field pressure, and to determine the far-field pressure directivity over a range of frequencies. For this purpose, we use a simplified representation for Lighthill's turbulence tensor. In particular, $\tilde{T}_{12}$ and $\tilde{T}_{21}$ are assumed to be the only nonzero components and are given by

$$\tilde{T}_{12}(\boldsymbol{x})=\tilde{T}_{21}(\boldsymbol{x})=\tfrac{1}{2}H(a-|\boldsymbol{x}-\boldsymbol{R}_0|)\delta(z-0) \tag{24}$$

Thus, the acoustic sources are 1–2 and 2–1 quadrupole distributions that are nonzero over a circle of radius a centered around the point $\boldsymbol{R}_0$. The vector $\boldsymbol{R}_0$ represents the displacement of the sources from the trailing edge. In the present example, we have chosen $a=0.001$ and $\boldsymbol{R}_0=[0,0.008,0]^T$. The mesh consists of 111,416 linear triangular finite elements and 55,708 nodes.

We have computed noise generated by this source distribution at several frequencies. For these calculations the ratio of the chord to the acoustic wavelength (L/λ) is between $\frac{1}{8}$ and 4. We have compared our far-field numerical solution with two analytical solutions. In the short-chord limit $L\ll\lambda$, the analytical solution is obtained using Curle's formulation[21] and is given by

$$\tilde{p}(\bar{r},\theta,0)=\frac{ik}{4\pi}\frac{e^{ik\bar{r}}}{\bar{r}}\left(\cos\theta\int_\Gamma p_C n_x\,\mathrm{d}\Gamma+\sin\theta\int_\Gamma p_C n_y\,\mathrm{d}\Gamma\right) \tag{25}$$

where $p_C(r,\theta)=\hat{p}(r,\theta,\gamma=\pm k)$ represents the incompressible solution to the original problem evaluated at $k_\gamma=0$. In the long-chord limit $L\gg\lambda$, the analytical solution is due to Ffowcs Williams and Hall.[8] In this case the airfoil is approximated by a semi-infinite plate, and the far-field acoustic pressure is given by

$$\tilde{p}(\bar{r},\theta,0)=\frac{1+i}{2(2\pi)^{\frac{3}{2}}}\frac{\sqrt{k}}{(k|\boldsymbol{R}_0|)^{\frac{3}{2}}}\frac{e^{ik\bar{r}}}{\bar{r}}\sin\frac{\theta}{2} \tag{26}$$

In Figs. 1–5, we show results for the model problem. Figures 1a–5a represent the near-field value of the real component of $\hat{p}$. These figures provide insight into the influence of the structure in determining the far-field pressure. The imaginary part of the field is not shown because it is similar to the real part. Figures 1b–5b are polar plots of the absolute value of the pressure at a radius of 30 chord lengths from the trailing edge on the $z=0$ plane, as a function of θ, that is, $|\tilde{p}(30,\theta,0)|$ vs θ. To quantify the effect of the airfoil on the far-field noise, we have also shown the pressure induced by the quadrupole source in free space (denoted by $\tilde{p}_I$) and the difference

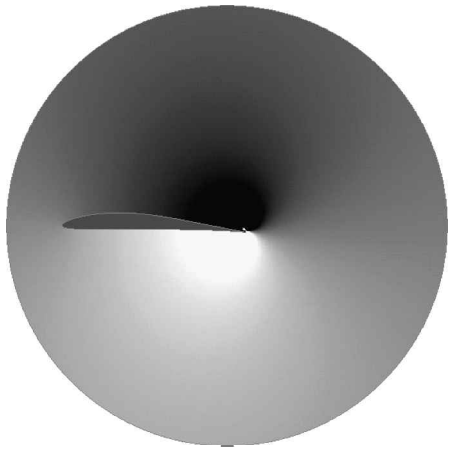

a) Real part of the near-field pressure

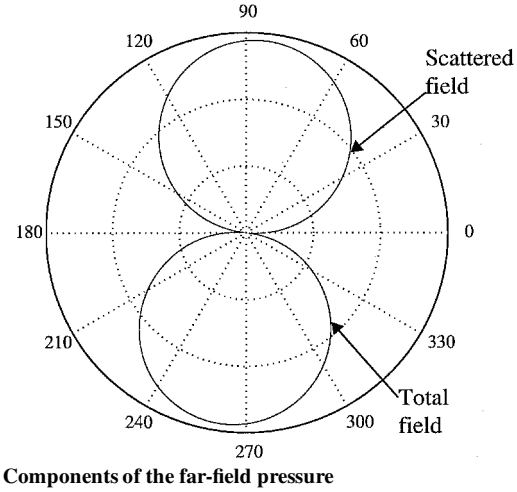

b) Components of the far-field pressure

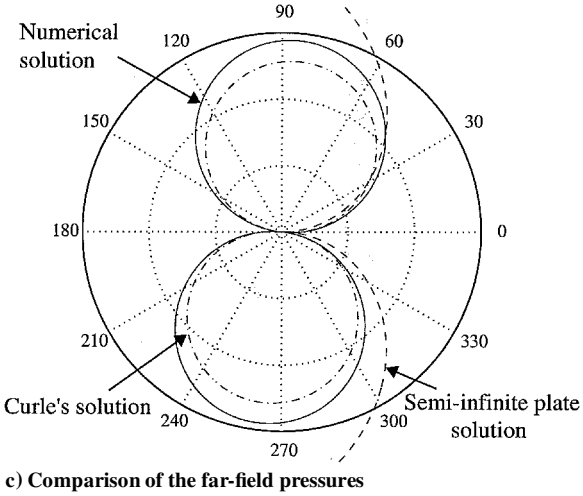

c) Comparison of the far-field pressures

Fig. 1 Solution to the model problem for $L/\lambda = \frac{1}{8}$.

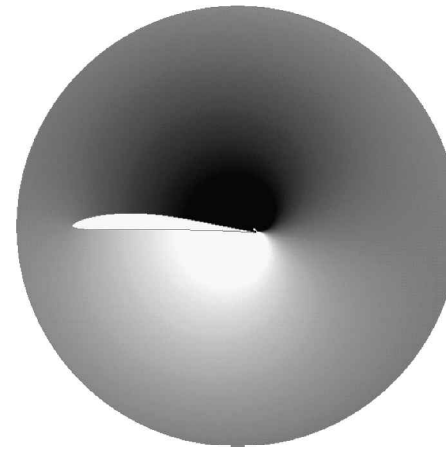

a) Real part of the near-field pressure

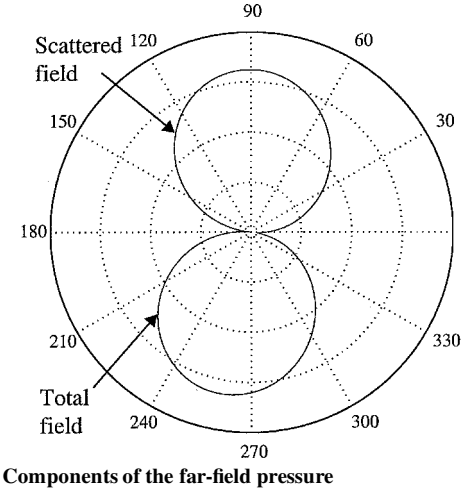

b) Components of the far-field pressure

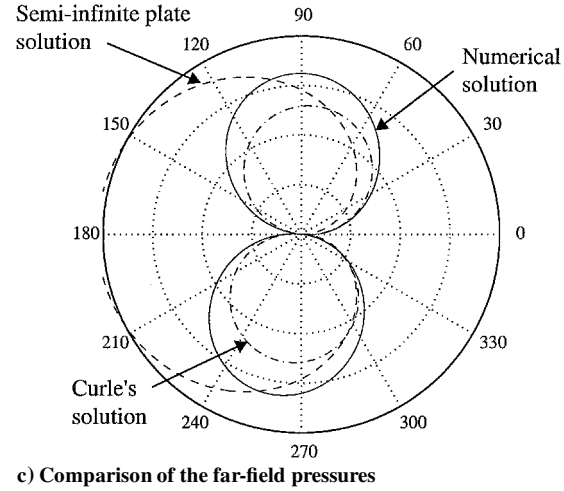

c) Comparison of the far-field pressures

Fig. 2 Solution to the model problem for $L/\lambda = \frac{1}{4}$.

(denoted by $\tilde{p}_S = \tilde{p} - \tilde{p}_I$). If we were to look at the airfoil as a scatterer, then $\tilde{p}_I$ represents the incident pressure and $\tilde{p}_S$ represents the scattered pressure. In Figs. 1c–5c, we have compared the absolute value of the far-field pressure obtained from our calculation with the pressures obtained using Eqs. (25) and (26). These comparisons have also been made as a function of θ, for $z = 0$, at a radius of 30 chord lengths from the trailing edge.

In Fig. 1 we present results for $L/\lambda = \frac{1}{8}$. For this case, the acoustic wavelength is much greater than the chord length, and the solution resembles a dipole oriented along the chord of the airfoil. This is clearly seen in Fig. 1a. We observe a region of negative pressure fluctuation above the airfoil (indicated by the dark tone) and a region of positive pressure fluctuation below the airfoil (indicated by the light tone). This situation is reversed for the imaginary component of the solution (not shown). An analysis of Fig. 1b reveals that the incident pressure, which represents the noise generated by the quadrupole in free space, is very small when compared with the total or the scattered acoustic pressure. In fact, the incident pressure field is so small that it cannot be seen in Fig. 1b. As a result, the total acoustic field is dominated by the scattered field, and the two are indistinguishable in Fig. 1b. In Fig. 1c, a comparison of the numerical solution with the two analytical estimates reveals that, for this value of L/λ, Curle's solution is very accurate and the semi-infinite plate solution is inaccurate, as might be anticipated.

In Fig. 2, we present results for $L/\lambda = \frac{1}{4}$. As for the preceding case, we observe that the total solution resembles a dipole oriented

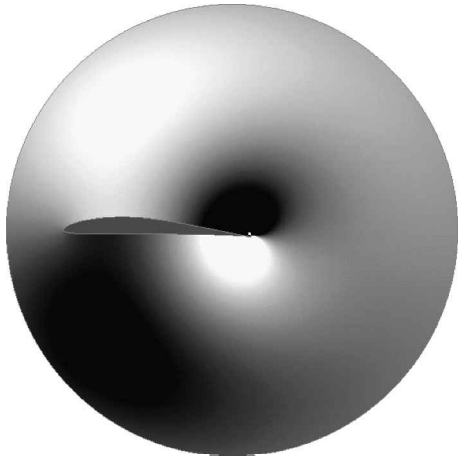

a) Real part of the near-field pressure

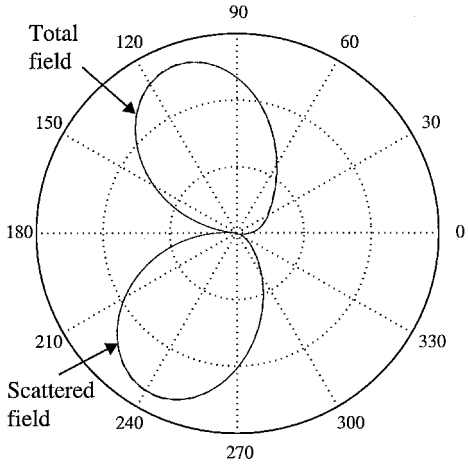

b) Components of the far-field pressure

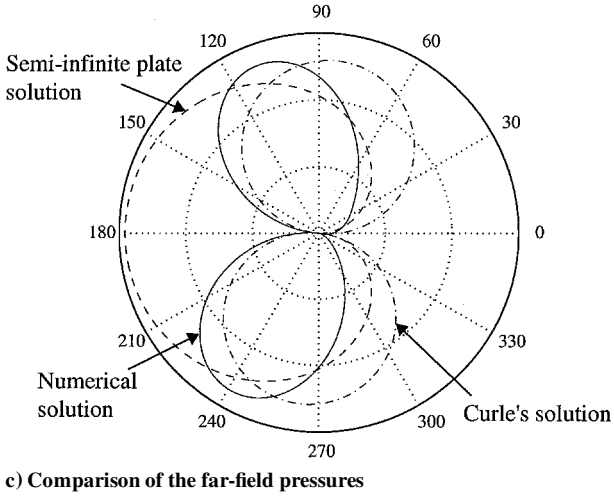

c) Comparison of the far-field pressures

Fig. 3 Solution to the model problem for $L/\lambda = \frac{1}{2}$.

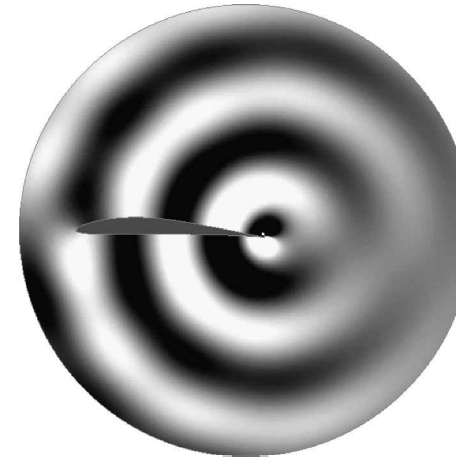

a) Real part of the near-field pressure

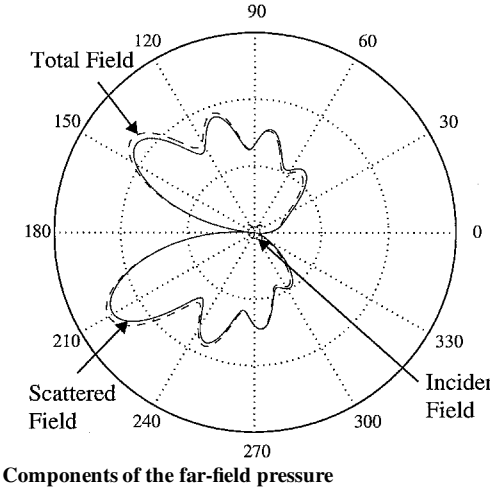

b) Components of the far-field pressure

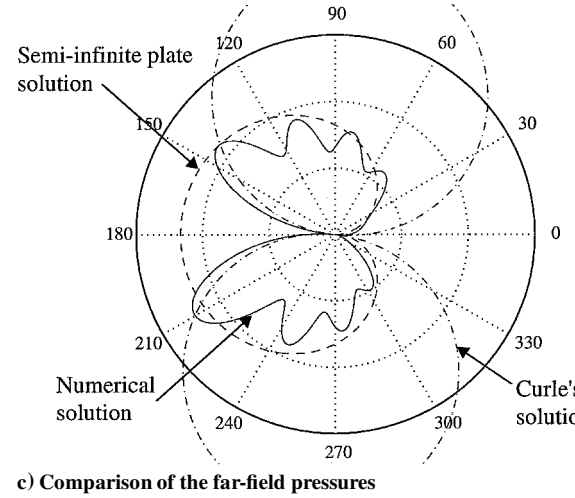

c) Comparison of the far-field pressures

Fig. 4 Solution to the model problem for $L/\lambda = \frac{2}{1}$.

along the chord of the airfoil and is completely dominated by the scattered component of the pressure (Figs. 2a and 2b). However, a comparison of the solution with Curle's solution shows that, although the directivity patterns match fairly well, there is greater discrepancy in the magnitude when compared with the preceding case.

In Fig. 3, we show results for $L/\lambda = \frac{1}{2}$. For this case, the acoustic wavelength and the chord length are comparable, and the solution changes significantly from the earlier two cases. On examining the real part of the solution near the airfoil (Fig. 3a), we observe that the directions corresponding to large pressure fluctuations are no longer perpendicular to the axis of the airfoil. They are tilted by about 30 deg toward the leading edge. This is also borne out by the directivity plot in Fig. 3b. In Fig. 3b, we observe again that for this case the major component of the far-field noise is the scattered pressure. The comparison in Fig. 3c reveals that the numerical solution is significantly different than both the Curle and the semi-infinite plate solutions.

Figure 4 contains results for $L/\lambda = \frac{2}{1}$. For this case, the wavelength is small when compared with the computational domain so that the wavelike behavior of the solution is clear (Fig. 4a). We observe that the solution consists of two wave trains that are out of phase and are generated on opposite sides of the trailing edge. These waves travel along the surface of the airfoil until they arrive at the leading edge, where they are diffracted. Also, at this point,

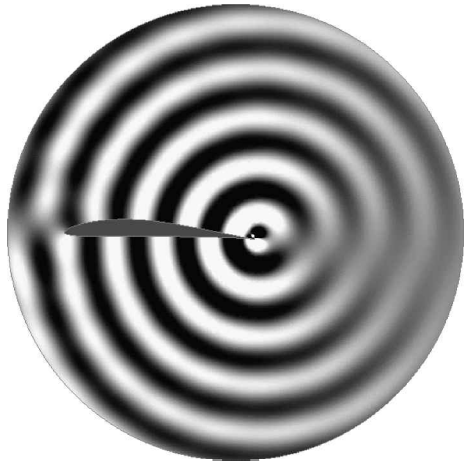

a) Real part of the near-field pressure

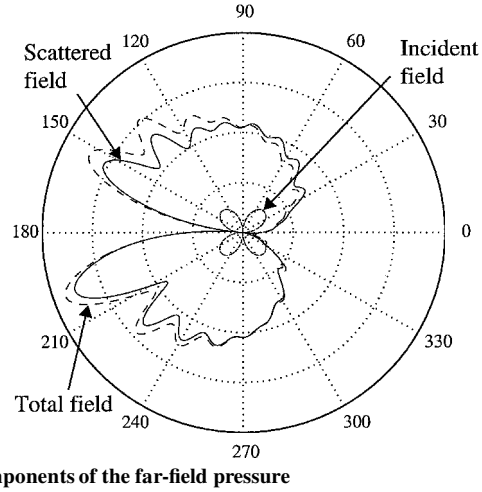

b) Components of the far-field pressure

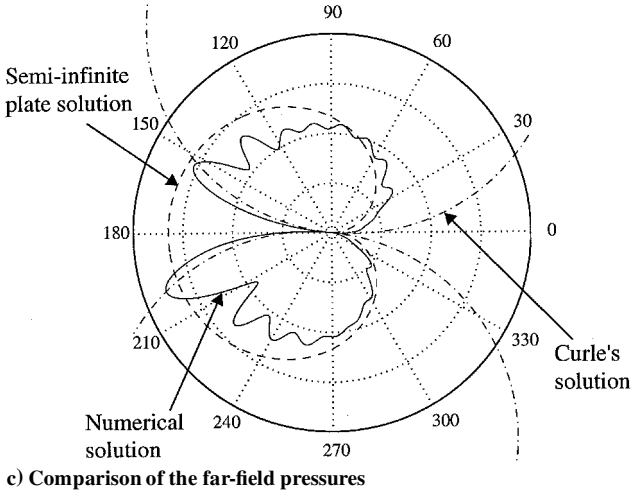

c) Comparison of the far-field pressures

Fig. 5 Solution to the model problem for $L/\lambda = \frac{4}{1}$.

a destructive interference leads to no noise being propagated in the upstream direction. The diffracted waves then travel in the upstream direction on the surface opposite to where they were generated. The interaction of these waves with the primary waves leads to the interference patterns seen in Fig. 4a. Once the diffracted waves arrive at the trailing edge, they are diffracted once again and so on. The numerical solution accounts for these repeated diffractions. The far-field directivity pattern is shown in Fig. 4b. In Fig. 4b, we observe for the first time that the incident field is large enough that there is a discernible difference between the scattered and the total field. However, it is still small when compared to the total field. A comparison with the analytical solutions (Fig. 4c) reveals that the numerical solution is very different from Curle's solution, which is to be expected because $L > \lambda$ for this case. However, it bears resemblance to the semi-infinite plate solution except in the following ways:

1) The numerical solution contains lobes formed by the interference of primary and secondary diffracted waves as described earlier.

2) The noise transmitted in the upstream direction is very small.

These features in the numerical solution are due to the finiteness of the chord, which is not taken into account in the semi-infinite plate solution.

Finally, in Fig. 5, we present results for $L/\lambda = \frac{4}{1}$. In this case, the solution is qualitatively similar to the preceding case. The notable differences are as follows:

1) The relative contribution from the incident field is greater. In Fig. 5b, we observe the quadrupole directivity associated with it. This increase in the contribution from the incident field can be understood by examining the results of Crighton and Leppington,[9] where it is shown that for a quadrupole source placed close to the trailing edge, the ratio of the scattered to the incident field varies as $(k|\boldsymbol{R}_0|)^{-3/2}$. Thus, for $|\boldsymbol{R}_0|$ fixed, increasing k (or reducing λ) reduces this quantity, thereby increasing the contribution from the incident field.

2) The direction of maximum noise shifts closer to the leading edge.

3) The directivity pattern is more asymmetric about the axis of the airfoil because the wavelength is now comparable to the thickness of the airfoil. The airfoil is asymmetric, and the thickness represents the order of asymmetry.

Remark: Recently, Howe[12] presented analytical results for the far-field pressure distribution associated with an airfoil of arbitrary chord. In his work he derived a composite Green's function valid for all values of L/λ by combining an approximate Green's function valid for $L > \lambda$ with another valid for $L < \lambda$. Note that our far-field directivities match his results remarkably well. Also, because we make no geometrical approximations, we believe that by performing a systematic study using our formulation the accuracy of the approximate Green's function proposed in Ref. 12 can be verified.

Trailing-Edge Noise from Turbulent Flow

In this section, we evaluate the far-field noise generated by turbulent flow over an Eppler 387 airfoil at an angle of attack of 2 deg. The Reynolds number based on freestream velocity and chord length is 1×10^5. Noise is computed by solving two problems: First, the incompressible Navier–Stokes equations are integrated in time to evaluate Lighthill's turbulence tensor. Second, the acoustic problem is solved to calculate the far-field pressure.

Fluid Calculation

In this calculation, the incompressible Navier–Stokes equations (1) and (2) are solved to evaluate Lighthill's turbulence tensor. For the Reynolds number considered (1×10^5 based on the chord length and freestream velocity), we expect the flow to be turbulent at least over some part of the airfoil. We chose to model turbulence using LES. We prefer LES over techniques based on Reynolds averaged Navier–Stokes equations because we are interested in the time-dependent fluctuations of Lighthill's turbulence tensor and not a time-averaged response. To model the effect of the subgrid scales, we employ the dynamic Smagorinsky eddy viscosity model of Germano et al.[22] To construct the two velocity scales required to determine the eddy viscosity within this framework, we use the generalized top-hat filter.[23] For a detailed description of the dynamic Smagorinsky model see Refs. 24 and 25, and for the application of this model to unstructured meshes see Refs. 26 and 27. In what follows, we briefly describe the results of the fluid calculation. The details of this calculation may be found in Ref. 28.

Preliminaries

We solve the spatially filtered form of the incompressible Navier–Stokes equations. In these equations the unbounded domain Ω is replaced by a truncated computational domain $\Omega_f = [-3, 2] \times [-2, 2] \times [-0.04, 0.04] \cap \Omega$. Recall that the x and z coordinates represent the streamwise and spanwise directions, respectively, and that the chord length of the airfoil is chosen to be unity.

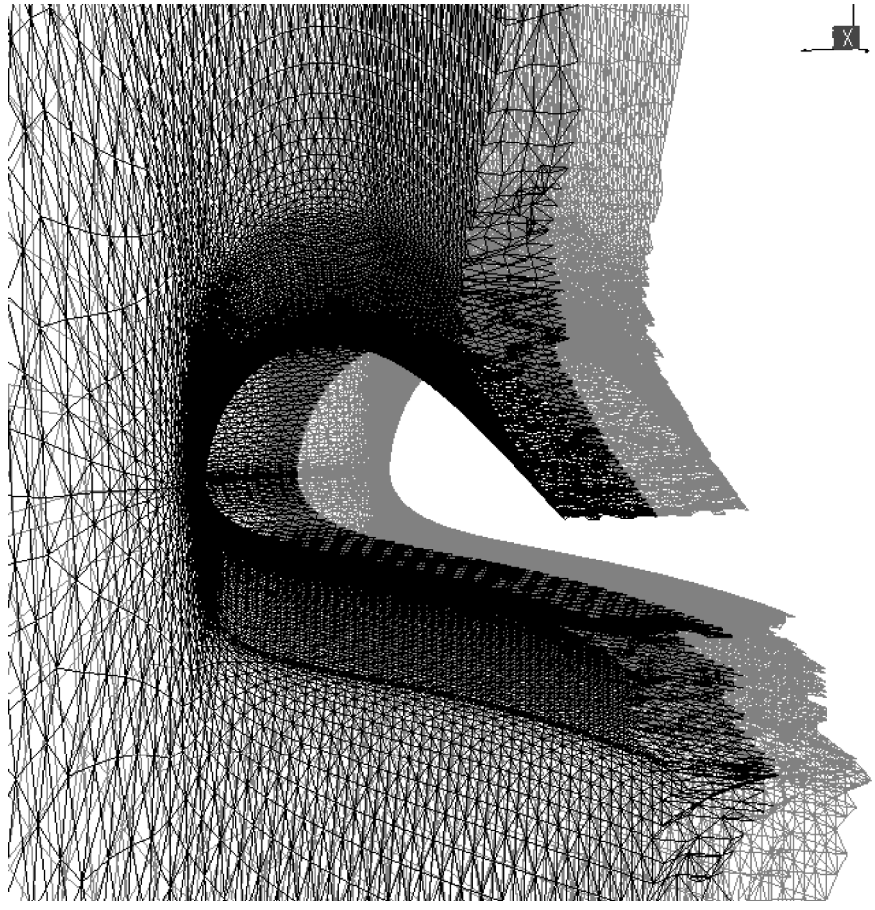

Fig. 6 Spanwise cut showing the unstructured mesh.

Boundary conditions for the LES calculation are as follows: At the inlet ($x = -3$), we impose a freestream boundary condition, that is, $u = u_\infty$ and $v = w = 0$. On top and bottom surfaces ($y = -2, 2$), we impose zero velocity, that is, $u = v = w = 0$. At the outlet ($x = 2$), we impose a zero-traction boundary condition. On the surface of the airfoil, we impose a no-slip boundary condition, that is, $u = v = w = 0$. On the faces perpendicular to the spanwise direction ($z = -0.04$ and 0.04), we impose periodic boundary conditions. The periodic boundary conditions imply that there is homogeneity in the spanwise direction and that we are effectively modeling an airfoil that is infinite in the spanwise direction. Another consequence of this boundary condition is that all components of Lighthill's tensor are periodic in the z direction. As a result, the contribution from components of the tensor involving a spanwise derivative, namely, T_{13}, T_{31}, T_{23}, T_{32}, and T_{33}, is zero. Thus, the source term in Eq. (23) for $\gamma = 0$ is given by

$$(\nabla w, \nabla \cdot \hat{\boldsymbol{T}}) = \int_{\bar{\Omega}} w_{,i} \hat{T}_{ij,j}(x, y, 0)\, \mathrm{d}\Omega, \qquad i, j = 1, 2 \quad (27)$$

where

$$\hat{T}_{ij}(x, y, 0) = \int_{-0.04}^{0.04} \tilde{T}_{ij}(x, y, z)\, \mathrm{d}z \quad (28)$$

The fluid mesh consists of 2.6×10^6 tetrahedral elements and 618,746 nodes. It is unstructured with relative coarsening in all three directions away from the leading edge and regions of turbulent flow. These regions are known a priori from previous experimental and computational studies.[29,30] In particular, we expect the flow to be turbulent in a region over the upper surface, beginning at approximately 20% of the chord length from the trailing edge and extending in the downstream direction into the wake. With this in mind, we have used 61 mesh points on the lower surface and 240 mesh points on the upper surface. Most of the points are clustered near the leading edge and the trailing edge. In the turbulent boundary-layer region, we have used 65 grid points in the wall-normal direction placed according to a hyperbolic tangent function. The thickness of the boundary layer is approximately 0.06 units. This estimate was obtained from Refs. 31 and 32. In the spanwise direction, we have used 17 points in the turbulent boundary layer and wake regions. This number is reduced in other parts of the domain. In Fig. 6, we have shown the mesh along a cut near the trailing edge. In Fig. 6, mesh refinement near the leading edge, the trailing edge, and in the wake regions may be seen.

The mesh parameters can be expressed in the wall units once the simulation is complete. For our calculation, in the turbulent boundary-layer regions, they are $\Delta x^+ \approx 10$, $0.7 < \Delta \eta^+ < 10$, and $\Delta z^+ \approx 20$, where x, η, and z are the streamwise, the wall-normal, and the spanwise directions, respectively. Furthermore, the plus length scale is related to the physical length scale by way of the relation $l^+ = l\langle u_\tau \rangle / (\mu / \rho_\infty)$, where $\langle u_\tau \rangle$ is the span- and time-averaged value of the skin-friction velocity u_τ. All mesh parameters are within the accepted range for LES calculations (for example, Ref. 33).

Computational Results

The LES calculation was performed on eight 195-MHz processors of an Origin 2000 computer. The initial condition for the three-dimensional problem was obtained from a two-dimensional calculation at the same Reynolds number. The two-dimensional solution displayed periodic vortex shedding and a long, relatively undamped vortex street. In the three-dimensional calculation, these large vortices were replaced by smaller eddies and a turbulent boundary layer near the trailing edge. Specifically, on the upper surface of the airfoil, immediately after the leading edge, there is a region where the flow accelerates and then detaches at about 40% of the chord from the leading edge. Large vortices are created in the primary separated region, which extends to about 15% of the chord beyond the separation point. In the rest of the separation region, these vortices break down, and the flow transitions to turbulence. The flow reattaches at about 80% of the chord from the leading edge. Thereafter,

Table 1 Comparison of computed and experimental values[29] of the separation and reattachment points

Method	Separation point (x/C)	Reattachment point (x/C)
Computed	0.42	0.84
Experiment	0.40	0.79

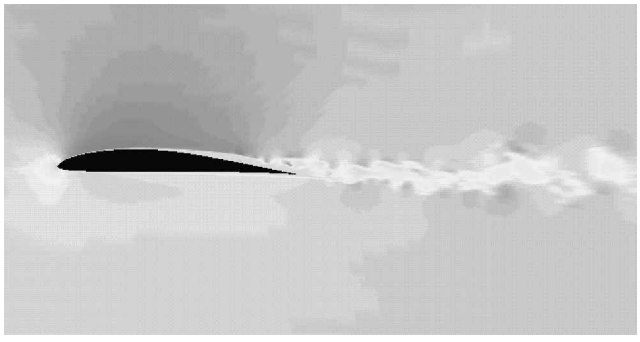

Fig. 7 Snapshot of streamwise velocity on the $z = 0$ plane.

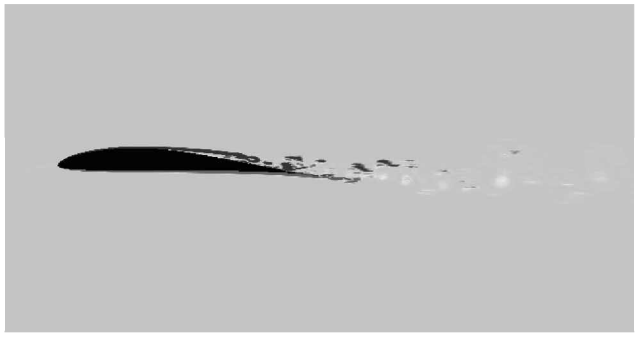

Fig. 8 Snapshot of spanwise vorticity on the $z = 0$ plane.

a turbulent boundary layer is observed leading to a wake that is also turbulent. Over the lower surface of the airfoil, the flow is laminar and remains attached throughout. These features of the flow can be seen in the snapshots of streamwise velocity and spanwise vorticity (Figs. 7 and 8, respectively) on the $z = 0$ plane.

The statistics for the turbulent solution took about 1000 time steps to converge. This corresponds to about 4.5 flow-through times based on the chord length. Thereafter, we solved the flow equations for an additional 900 time steps during which values of velocities and pressure were recorded. These were used to construct the components of Lighthill's turbulence tensor and for comparisons with experimental results.

In Table 1, we have compared time- and span-averaged values of the separation and reattachment points obtained from our calculation with experimental results.[29] Although the agreement is quite good, the computed values are somewhat offset toward the downstream direction. This slight discrepancy can be ascribed to the inability of the computational scheme to resolve the early instability waves and also to the relatively small spanwise length used in our simulation. (See Ref. 28 for a detailed discussion.) Figure 9 is the plot of $C_p = (\langle p \rangle - p_\infty)/(\rho_\infty u_\infty^2/2)$ for this problem. The solid line represents values from the calculation and the symbols represent the experimental data.[29] The agreement is excellent. By examining the pressure distribution in the region close to the trailing edge, we observe that the turbulent boundary layer develops under an adverse pressure gradient.

Acoustic Calculation

In this calculation, we determine the far-field acoustic pressure for the flow described in the preceding section. The source terms that appear in the acoustic problem are components of Lighthill's tensor and are given by Eq. (6). For the problem considered, most sources are located in the turbulent region of the flow. This region

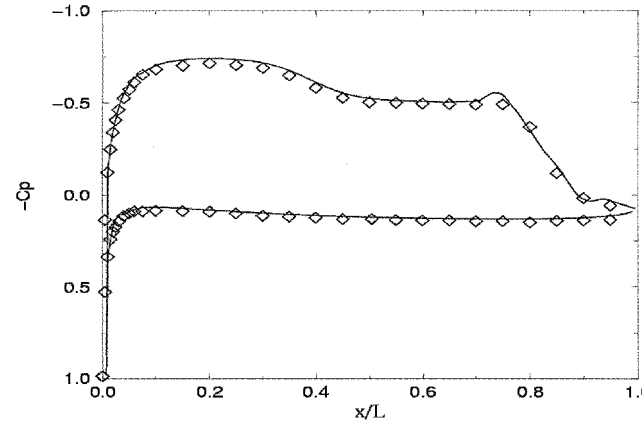

Fig. 9 Average pressure coefficient around the airfoil: ——, computed and ◇, experimental data.[29]

begins at about 15% of the chord length from the trailing edge in the upstream direction and extends well into the wake in the downstream direction. Based on this observation and the results of the model problem, we expect the trailing edge to play an important role in determining the sound radiated to the far field.

Preliminaries

The velocity field obtained from the fluid calculation was used to construct Lighthill's turbulence tensor. For this purpose, velocity data were collected for 900 time steps after statistical steady state was achieved. From these data, eight time series, each comprising 200 time steps, were constructed. These sets contained the values of turbulence tensor from time step $(i-1) \times 100$ to $(i-1) \times 100 + 200$, for $i = 1, \ldots, 8$. The components of the turbulence tensor were multiplied with a Hanning window function to make them periodic in that time interval. Thereafter, the turbulence tensor was transformed to the frequency domain by performing a discrete Fourier transform. For each time series, contributions from the 18 lowest harmonics were analyzed. The Mach number for the problem was chosen to be 0.1. The nondimensional circular frequency ω (nondimensionalized by u_∞/L) was in the range from 8.4 to 150.8, and the ratio L/λ was in the range from 0.13 to 2.4. Thus, the acoustic wavelength varied from being much larger than the chord length to much smaller. The acoustic mesh used was the same as for the earlier example.

Remark: We have used more than one time series in our analysis because the acoustic problem is driven by turbulent sources, and, therefore, we expect significant variations in the computed acoustic pressure at a given frequency, from one realization (200-step time series) to another. Furthermore, the phase of the acoustic pressure will be random, and in the limit of an infinite number of realizations its average will tend zero. As a result, the prime quantity of interest is the average value (over all of the realizations) of the absolute value of pressure at a given spatial location and frequency.

Computational Results

In Figs. 10–14, we have plotted the absolute value of the scattered pressure on the $z = 0$ plane, at a fixed radius of 30 chord lengths, as a function of the polar angle θ. These are the directivity plots on this plane. As before, the scattered pressure is obtained from the total pressure by subtracting the incident pressure, which is the pressure generated by turbulence in free space, that is, with the airfoil removed. We have chosen to examine the directivity of the scattered pressure as opposed to the total pressure for the following reasons:

1) The incident pressure has no preferred direction associated with it; thus, the scattered pressure represents the component of the total solution exhibiting directional dependence.

2) For most frequencies considered, the scattered pressure is the major component of the total field.

In each of Figs. 10–14, the dotted lines represent results from a single realization and the solid line represents the average. For the lowest frequencies (Fig. 10), the scattered field looks very much like a dipole oriented along the axis of the airfoil. This is to be expected

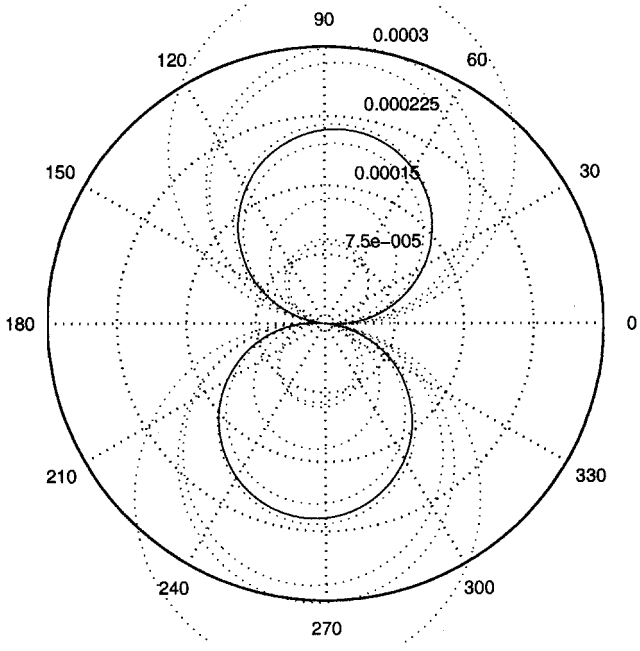

Fig. 10 Far-field pressure directivity for the turbulent flow problem: $\omega = 8.4$ and $L/\lambda = 0.13$.

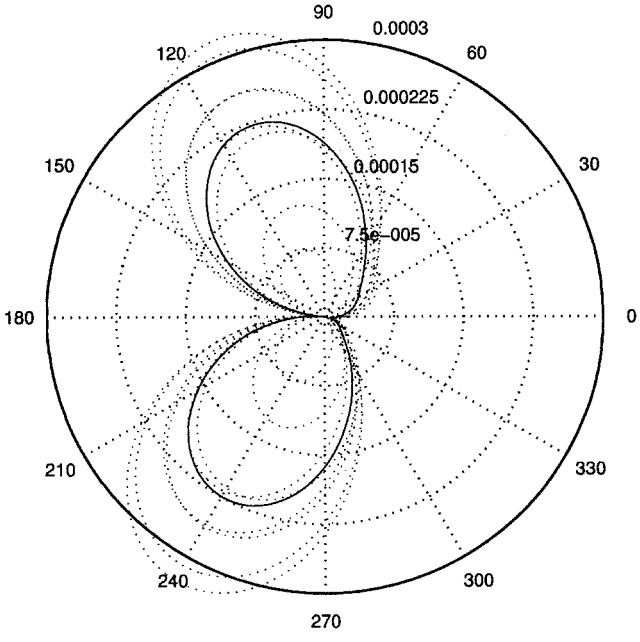

Fig. 11 Far-field pressure directivity for the turbulent flow problem: $\omega = 33.5$ and $L/\lambda = 0.53$.

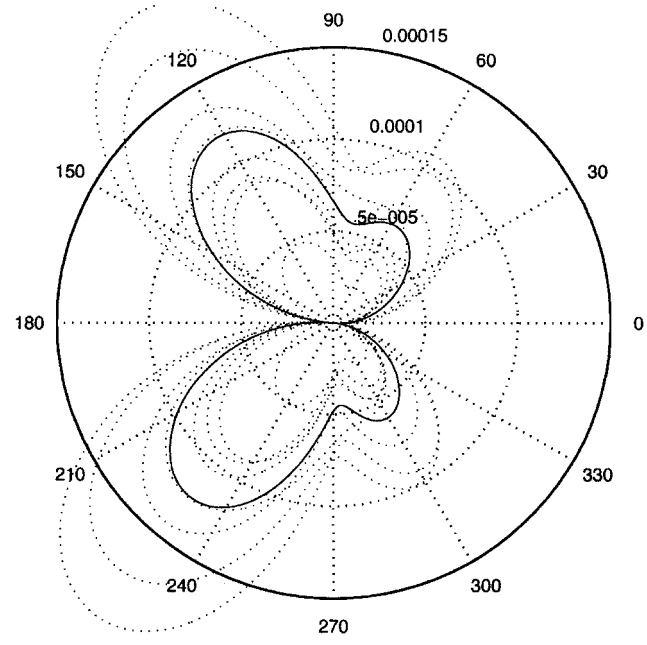

Fig. 12 Far-field pressure directivity for the turbulent flow problem: $\omega = 50.3$ and $L/\lambda = 0.80$.

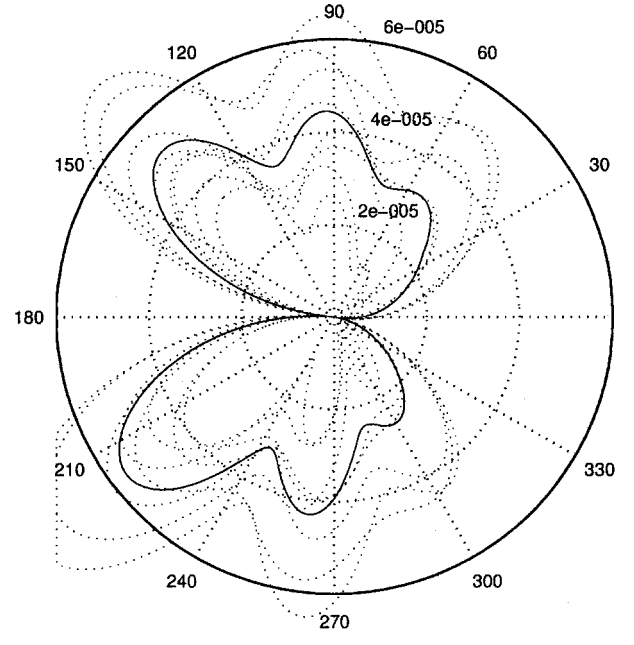

Fig. 13 Far-field pressure directivity for the turbulent flow problem: $\omega = 92.1$ and $L/\lambda = 1.46$.

because for $L/\lambda \ll 1$ Curle's formulation indicates that, irrespective of the shape of the scatterer, the far-field solution will be in the form of a dipole.

For higher values of ω (Fig. 11), the direction of maximum noise shifts toward the leading edge, and the directivity begins to depart from the form of a dipole. These values correspond to cases where the short-chord hypothesis made in Curle's formulation is no longer valid.

When $L/\lambda > 0.6$ (Fig. 12), in addition to the shift of the direction of maximum noise toward the leading edge, we observe the appearance of secondary lobes in the directivity patterns. As described earlier, these lobes are a result of the interference between primary scattered waves generated at the trailing edge and the secondary scattered waves scattered by the leading edge.

For higher values of ω (Fig. 13), the solution tends toward the $\sin(\theta/2)$ directivity pattern associated with the diffraction of the field generated by a quadrupole source placed close to a semi-infinite rigid plate; compare Eq. (26). However, there are two significant differences, namely, the lobes and a low value of intensity for $\theta = \pi$. These can be ascribed to the finiteness of the chord, as explained in the preceding section.

For higher frequencies (Fig. 14), the far-field pattern is somewhat different from that for diffraction of a quadrupole source by either a finite chord airfoil or a semi-infinite plate. (See Fig. 4c for the directivity associated with these cases.) The solution in Fig. 14 appears to have other contributions. This may be understood as follows: In addition to the trailing-edge noise due to diffraction, the scattered field ($\tilde{p}_S$) contains contributions from the specular reflection of quadrupoles by the airfoil surface. That is,

$$\tilde{p}_S = \tilde{p}_R + \tilde{p}_D \tag{29}$$

where $\tilde{p}_R$ is the pressure due to reflection and $\tilde{p}_D$ is the pressure due to diffraction. In the high-frequency limit, the reflected field is

simply the noise due to image quadrupole sources placed below the airfoil; hence,

$$|\tilde{p}_R|/|\tilde{p}_I| \approx \mathcal{O}(1) \tag{30}$$

where $\tilde{p}_I$ is the incident pressure. In the same limit we have

$$|\tilde{p}_D|/|\tilde{p}_I| \approx \mathcal{O}\left[(k|\boldsymbol{R}_0|)^{-\frac{3}{2}}\right] \tag{31}$$

(for example, see Ref. 9). From Eqs. (30) and (31) we have

$$|\tilde{p}_D|/|\tilde{p}_R| \approx \mathcal{O}\left[(k|\boldsymbol{R}_0|)^{-\frac{3}{2}}\right] \tag{32}$$

In our case, $|\boldsymbol{R}_0|$ is fixed as a function of ω; however, as $k = \omega M$ increases, the scattered noise component due to the diffraction decreases when compared with the component due to reflection. This leads to a directivity pattern that departs from $\sin(\theta/2)$. This explanation is consistent with the observation that even for high frequencies the amplitude of the scattered field along the axis of the airfoil is very small because both the diffracted and reflected contributions vanish along this direction.

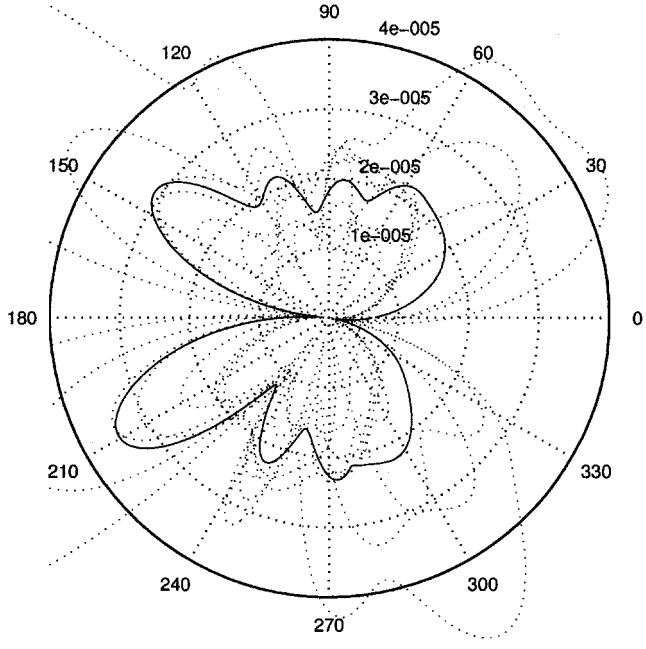

Fig. 14 Far-field pressure directivity for the turbulent flow problem: $\omega = 142.4$ and $L/\lambda = 2.26$.

Finally, in Fig. 15 we have plotted $\bar{p}$, the average (over eight realizations and over θ) of the absolute value of pressure, on a circle on the $z = 0$ plane at a radius of 30 chord lengths from the trailing edge, that is, $\bar{p}$ is given by

$$\bar{p} = \left\langle\!\!\left\langle \frac{1}{2\pi}\int_0^{2\pi} |\tilde{p}(30\cos\theta, 30\sin\theta, 0)|\,\mathrm{d}\theta \right\rangle\!\!\right\rangle \tag{33}$$

where $\langle\!\langle \cdot \rangle\!\rangle$ denotes average over eight realizations. In Fig. 15, we have plotted both the scattered and the total values of pressure as a function of the nondimensional frequency ω. We observe that there is a peak in the far-field noise at $\omega \approx 15$. This value is close to the vortex shedding frequency. We also observe that with increasing frequency the total and the scattered values diverge. As explained in the preceding paragraph, this may be ascribed to the weakening of the diffraction component of the trailing-edge noise source relative to the incident field.

Conclusions

We have applied the variational formulation of Lighthill's acoustic analogy (see Ref. 1) to the trailing-edge noise problem. We have considered two problems:

1) In the first problem we determined the acoustic field generated by a simple quadrupole source placed close to the trailing edge of a finite-chord Eppler airfoil. We made two observations:

a) Over the frequency range considered, the scattered component of the far-field acoustic pressure is much greater than the incident component. This observation highlights the role of the airfoil in amplifying the noise radiated to the far-field.

b) In the low-frequency regime, the far-field pressure directivity resembles that for a dipole, and the results are in good agreement with Curle's formulation. In the high-frequency regime, the results exhibit features in common with a semi-infinite plate solution, but differences exist that may be ascribed to finiteness of the chord. We also studied the transition of the directivity from low to high frequencies.

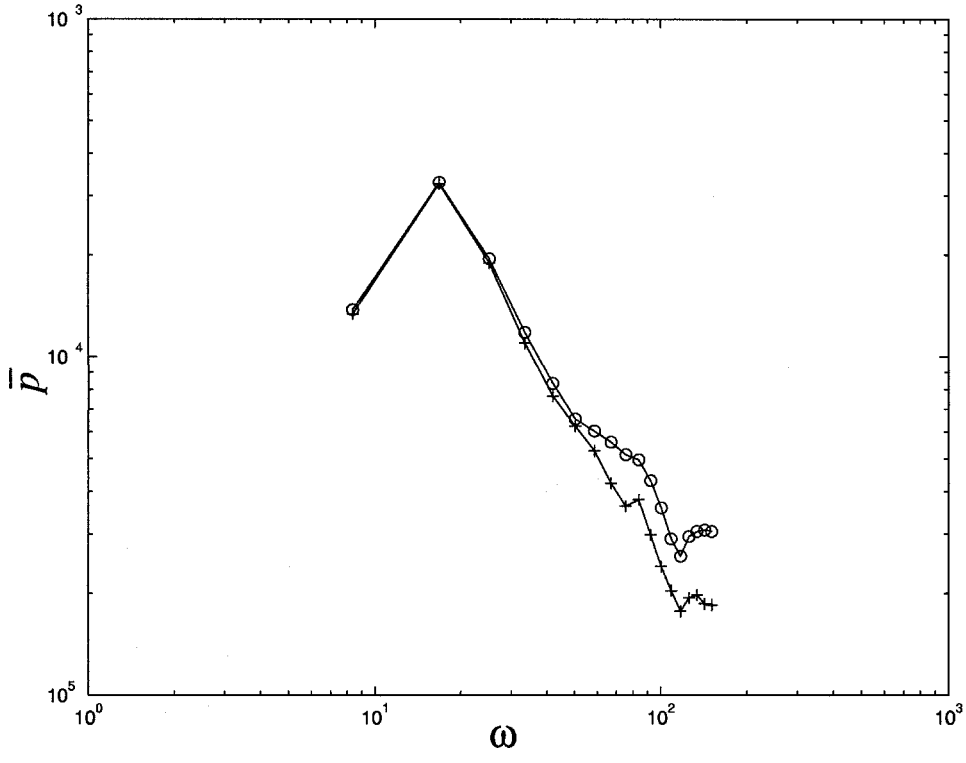

Fig. 15 Absolute value of the integrated far-field acoustic intensity vs ω for the turbulent flow problem.

2) In the second problem, for the same airfoil, we computed the far-field acoustic pressure generated by a turbulent flow. To determine the acoustic sources, we performed an LES using the dynamic Smagorinsky eddy viscosity model. We found that the major sources of noise are concentrated in the turbulent region near the trailing edge. Acoustic calculations revealed that, in the low- to midfrequencyrange, the far-field noise is dominated by the scattered field component and the directivity is consistent with that obtained for the model problem. In the high-frequency regime, the scattered field associated with the diffraction of the quadrupole noise weakens, and the incident component, that is, the noise generated by the same turbulence in free space, is found to be comparable to the scattered noise.

Based on our results, we conclude that the variational approximation of Lighthill's acoustic analogy in conjunction with LES can be used successfully to compute noise generated by low-Mach-number, turbulent flows. In future works, we plan to use this methodology to solve the trailing-edge noise problem for flexible airfoils and other challenging problems in aeroacoustics.

Acknowledgments

The support of NASA Ames Research Center Cooperative Agreement NCC 2-5363 and Office of Naval Research Grant 00014-99-1-0122 is gratefully acknowledged.

References

[1]Oberai, A. A., Roknaldin, F., and Hughes, T. J. R., "Computational Procedures for Determining Structural Acoustic Response due to Hydrodynamic Sources," *Computer Methods in Applied Mechanics and Engineering*, Vol. 190, No. 3–4, 2000, pp. 345–361.

[2]Lighthill, M. J., "On Sound Generated Aerodynamically I. General Theory," *Proceedings of the Royal Society of London, Series A: Mathematical and Physical Sciences*, Vol. 211A, No. 1107, 1952, pp. 564–587.

[3]Lighthill, M. J., "On Sound Generated Aerodynamically II. Turbulence as a Source of Sound," *Proceedings of the Royal Society of London, Series A: Mathematical and Physical Sciences*, Vol. 222, No. 1148, 1954, pp. 1–32.

[4]Ffowcs Williams, J. E., and Hawkings, D. L., "Sound Generation by Turbulence and Surfaces in Arbitrary Motion," *Philosophical Transactions of the Royal Society of London, Series A: Mathematical and Physical Sciences*, Vol. 264, No. 1151, 1969, pp. 321–342.

[5]Brentner, K. S., and Farassat, F., "Analytical Analysis of the Acoustic Analogy and Kirchhoff Formulation for Moving Surfaces," *AIAA Journal*, Vol. 36, No. 8, 1998, pp. 1379–1386.

[6]Singer, B. A., Brentner, K. S., Lockard, D., and Lilley, G. M., "Simulation of Acoustic Scattering from a Trailing Edge," *Journal of Sound and Vibration*, Vol. 230, No. 3, 2000, pp. 541–560.

[7]Howe, M. S., "Trailing Edge Noise at Low Mach Numbers," *Journal of Sound and Vibration*, Vol. 225, No. 2, 1998, pp. 211–238.

[8]Ffowcs Williams, J. E., and Hall, L. H., "Aerodynamic Sound Generation by Turbulent Flow in the Vicinity of a Scattering Half Plane." *Jounal of Fluid Mechanics*, Vol. 40, No. 4, 1970, pp. 657–670.

[9]Crighton, D. G., and Leppington, F. G., "On the Scattering of Aerodynamic Noise," *Journal of Fluid Mechanics*, Vol. 46, No. 3, 1971, pp. 577–597.

[10]Chase, D. M., "Sound Radiated by Turbulent Flow off a Rigid Half-Plane Obtained from a Wavevector Spectrum of Hydrodynamic Pressure," *Journal of the Acoustical Society of America*, Vol. 52, No. 3, 1971, pp. 1101–1123.

[11]Chandiramni, K. L., "Diffraction of Evanescent Waves, with Applications to Aerodynamically Scattered Sound and Radiation from Unbaffled Plates," *Journal of Acoustical Society of America*, Vol. 55, No. 1, 1973, pp. 18–29.

[12]Howe, M. S., "Edge-Source Acoustic Green's Function for an Airfoil of Arbitrary Chord, with Application to Trailing-Edge Noise," *Quarterly Journal of Mechanics and Applied Mathematics*, Vol. 54, No. 1, 2001, pp. 139–155.

[13]Holmes, B. S., Dias, J. B., Jaroux, B. A., Sassa, T., and Ban, Y., "Predicting the Wind Noise from the Pantograph Cover of a Train," *International Journal for Numerical Methods in Fluids*, Vol. 24, No. 12, 1997, pp. 1307–1319.

[14]Manoha, E., Troff, B., and Sagaut, P., "Trailing-Edge Noise Prediction Using Large-Eddy Simulation and Acoustic Analogy," *AIAA Journal*, Vol. 38, No. 4, 2000, pp. 575–583.

[15]Wang, M., and Moin, P., "Computation of Trailing-Edge Flow and Noise Using Large-Eddy Simulation," *AIAA Journal*, Vol. 38, No. 12, 2000, pp. 2201–2209.

[16]Abramowitz, M., and Stegun, I. A., *Handbook of Mathematical Functions*, 9th ed., Dover, New York, 1970.

[17]Junger, M. C., and Feit, D., *Sound, Structures, and Their Interaction*, 2nd ed., MIT Press, Cambridge, MA, 1985, pp. 175, 176.

[18]Keller, J. B., and Givoli, D., "Exact Non-Reflecting Boundary Conditions," *Journal of Computational Physics*, Vol. 82, No. 1, 1989, pp. 172–192.

[19]Freund, R. W., and Nachtigal, N. M., "QMR: A Quasi-Minimal Residual Method for Non-Hermitian Linear Systems," *Numerische Mathematik*, Vol. 60, No. 3, 1991, pp. 315–339.

[20]Oberai, A. A., Malhotra, M., and Pinsky, P. M., "Implementation of the Dirichlet-to-Neumann Radiation Condition for Iterative Solution of the Helmholtz Equation," *Applied Numerical Mathematics*, Vol. 27, No. 4, 1998, pp. 443–464.

[21]Curle, N., "The Influence of Solid Boundaries on Aerodynamic Sound," *Proceedings of the Royal Society of London, Series A: Mathematical and Physical Sciences*, Vol. 231, No. 1187, 1955, pp. 505–514.

[22]Germano, M., Piomelli, U., Moin, P., and Cabot, W., "A Dynamic Subgrid-Scale Eddy Viscosity Model," *Physics of Fluids*, Vol. 3, No. 7, 1991, pp. 1760–1765.

[23]Jansen, K. E., "Unstructured Grid Large Eddy Simulation of Flow over an Airfoil," TR, Center for Turbulence Research, CTR Annual Research Briefs, Stanford Univ./NASA Ames Research Center, Stanford, CA, 1994.

[24]Ghosal, S., Lund, T., Moin, P., and Akselvoll, K., "A Dynamic Localization Model for Large-Eddy Simulation of Turbulent Flows," *Journal of Fluid Mechanics*, Vol. 286, 1995, pp. 229–255.

[25]Lilly, D., "A Proposed Modification of the Germano Subgrid-Scale Closure Method," *Physics of Fluids A*, Vol. 4, No. 3, 1992, pp. 633–635.

[26]Jansen, K. E., "Large-Eddy Simulations of Flow Around a NACA 4412 Airfoil Using Unstructured Grids," TR, Center for Turbulence Research, CTR Annual Research Briefs, Stanford Univ./NASA Ames Research Center, Stanford, CA, 1996.

[27]Jansen, K. E., "Large-Eddy Simulation Using Unstructured Grids," *Advances in DNS/LES*, edited by C. Liu and Z. Liu, Greyden Press, Columbus, OH, 1997, pp. 117–128.

[28]Roknaldin, F., "Numerical Solution of Acoustic Response due to Hydro/Aerodynamic Turbulence," Ph.D. Dissertation, Div. of Mechanics and Computation, Stanford Univ., Stanford, CA, 2001.

[29]McGhee, R. J., Walker, B. S., and Millard, B. F., "Experimental Results for the Eppler 387 Airfoil at Low Reynolds Numbers in Langley Low-Turbulence Pressure Tunnel," NASA TM 4062, Oct. 1998.

[30]Lin, J. C. M., and Pauley, L. L., "Low-Reynolds-Number Separation on an Airfoil," *AIAA Journal*, Vol. 34, No. 8, 1996, pp. 1570–1577.

[31]Chen, H. H., Platzer, M. F., and Cebeci, T., "Analysis of Airfoils at Low Reynolds Numbers," *Seventh International Symposium on Unsteady Aerodynamics and Aeroelasticity of Turbomachines*, Fukuoka, Japan, Sept. 1994.

[32]Cebeci, T., Hefazi, H., Roknaldin, F., and Carr, L. W., "Predicting Stall and Post-Stall Behavior of Airfoils at Low Mach Numbers," *AIAA Journal*, Vol. 33, No. 4, 1995, pp. 595–602.

[33]Cabot, W., "Local Dynamic Subgrid-Scale Models in Channel Flow," TR, Center for Turbulence Research, CTR Annual Research Briefs, Stanford Univ./NASA Ames Research Center, Stanford, CA, 1994.

P. J. Morris
Associate Editor